Journal of Materials Chemistry B

ROYAL SOCIETY OF CHEMISTRY

PAPER

View Article Online
View Journal | View Issue

Cite this: J. Mater. Chem. B, 2022, 10, 5958

Catechol sensor based on pristine and transition metal embedded holey graphyne: a first-principles density functional theory study†

Seetha Lakshmy, [a] Ajit Kundu, [b] Nandakumar Kalarikkal*[acd] and Brahmananda Chakraborty *[ef]

Received 5th April 2022,
Accepted 5th July 2022

DOI: 10.1039/d2tb00754a

rsc.li/materials-b

To develop a highly sensitive and selective biosensor for detecting noxious biomolecules from the environment, we examined catechol (Cc) adsorption in pristine and transition metal (TM = Sc, Cu, and Pd) embedded 2D holey graphyne (hGY) monolayers using the first-principles density functional theory method. The interaction between Cc and the pristine hGY is purely weak, and hence the response of the sensing device will be difficult to detect. Therefore, the TM doping strategy is adopted to improve the sensitivity. According to our findings, Sc binds strongly to the hGY monolayer, with a binding energy of −4.09 eV and a charge transfer of 1.89*e* from the valence orbitals of Sc to the C 2p orbitals. Later on, the Cc adsorption on the TM-embedded hGY was investigated. The interaction of Cc with the transition metal involves charge transfer from Cc to the metal d orbital. A large binding energy of −3.22 eV and a significant charge transfer of about 0.9*e* from the O 2p orbitals of Cc to the valence orbital of Sc suggest that the Sc embedded hGY monolayer is a good choice for the efficient sensing of Cc molecules. Furthermore, *ab initio* MD simulations confirmed the structural stability of the Sc + hGY system at room temperature. We strongly believe that this theoretical work will aid the experimentalists in designing and developing 2D semiconducting nanolayer-based biosensors for commercial purposes.

Introduction

Over the recent years, the rapid advancement of science and technology to meet human needs has led to discoveries which have led to major environmental hazards.[1] Disposal of industrial effluents into the environment will have a massive impact and become toxic to land and aquatic life. Hence, identifying and removing harmful molecules from industrial effluents is paramount.[2] Most of the phenolic derivatives are toxic and non-biodegradable.[3] Catechol (or pyrocatechol), an isomer of phenol with the molecular formula $C_6H_5O_9$, is being used as the elementary raw material for manufacturing textiles, pesticides, pharmaceuticals, paints, cosmetics, plastics, *etc.*[4,5] Exposure to Cc during use or production can cause eczematous dermatitis in humans, and its overdose can induce depression and chronic high blood pressure, even in animals.[6–9] In this respect, accurate identification of Cc molecules is regarded as an effective method of avoiding their detrimental consequences.

Varied forms of Cc sensors such as optical, chemoresistive and electrochemical sensors have been developed to inspect and regulate the concentration of Cc in the environment.[10,11] A recently expanded fibre optic plasmonic sensor based on the CTAB/ZnO/CNTs nanocomposite (NC) deposited over the Ag thin film could quantify even trace amounts of Cc molecules in the real samples with a response time of 15 min.[12] In another study, Nsanzamahoro *et al.* prepared Si nanoparticles (NPs) *via* a simple water bath method as a novel choice for the fluorescence detection of Cc. The so prepared Si NPs show great sensitivity and selectivity towards Cc molecules in yellow river water, tap water, and human serum with a linear range from 0.06 to 40 μM and a detection limit of 20 nM. Furthermore, these Si NPs are thermally stable and can emit yellow-green fluorescence.[13] A biocompatible strain-induced chemoresistive Cc sensor based on 1D WO_3 nanofibers (NFs) was fabricated by

[a] International and Inter University Centre for Nanoscience and Nanotechnology, Mahatma Gandhi University, Kottayam, Kerala 686 560, India. E-mail: nkkalarikkal@mgu.ac.in
[b] Seismology Department, Bhabha Atomic Research Centre, Trombay, Mumbai 400085, India
[c] School of Pure and Applied Physics, Mahatma Gandhi University, Kottayam, Kerala 686 560, India
[d] School of Nanoscience and Nanotechnology, Mahatma Gandhi University, Kottayam, Kerala 686560, India
[e] High Pressure & Synchroton Radiation Physics Division, Bhabha Atomic Research Centre, Trombay, Mumbai 400085, India
[f] Homi Bhabha National Institute, Trombay, Mumbai 400085, India. E-mail: brahma@barc.gov.in

† Electronic supplementary information (ESI) available. See DOI: https://doi.org/10.1039/d2tb00754a

Veeralingam *et al.* The study showed that the large surface area with exposed surface-active sites of interconnected WO_3 NFs provides an enhanced sensitivity of 51.29 μM^{-1} cm^{-2} and an LOD of 0.52 μM towards the Cc molecule. This sensor material could selectively detect the Cc molecules from the blood samples.[14] Many effective techniques such as conventional chromatography and high-performance liquid chromatography have also been utilized for Cc sensing but necessitate expensive laboratory setup and hefty operations.[15] Other empirical methods, including voltametry,[16] colorimetric,[17] chemiluminescence,[18] *etc.*, have also been widely employed for Cc detection. Tedious pre-processing of the collected samples, less sensitivity and nuisance alarms limit the feasibility of these methods for the production of commercial sensors.

The presence of the hydroxy group makes the Cc molecule electroactive in nature. Therefore, the electrochemical technique is termed as the most convenient platform for its analysis.[19] A new polypyrrole/C black doped α-Fe_2O_3 (Ppy/CB/α-Fe_2O_3) NC based electrochemical Cc sensor constructed by Ahmed *et al.* displayed a superior sensitivity of 0.3521 μA μM^{-1} cm^{-2} over a wide range of 0.5–1188 μM with a LOD of 52.8 ± 0.1 nμ.[20] At the same time, Dang *et al.* prepared a pin needle-like nano $CePO_4$ modified carbon paste electrode ($CePO_4$/CPE) to examine the catalytic oxidation of Cc molecules. Simultaneously, the prepared $CePO_4$/CPE material could effectively sense trace Cc molecules in the linear range of 0.20–40 μM with a low detection limit of 0.1 μM. The proposed sensor material is highly reproducible and repeatable, and has excellent anti-interference properties against other similar species.[21] Zhao *et al.* have detailed the synthesis of NiO/CNT NC by layer deposition to detect electroactive molecules. The linear responses of this nanocomposite material towards Cc molecules were in the range of 10–400 μM, with a detection limit of 2.5 μM (S/N = 3).[22]

Several attempts have been made to design novel Cc sensors and are reviewed in the literature. Practically, it is really tough to seek extensive information about the sensing mechanism, such as most likely adsorption sites, adsorption configuration, binding energy, orbital interactions, charge transfer *etc.*, *via* laboratory experiments alone. The theoretical simulations can provide insights regarding orbital level molecular interaction, which not only help to understand the sensing mechanism but also provide data regarding sensing parameters to the experimental researchers for the successful development of the sensing devices with maximum performance. Many theoretical studies have been carried out simultaneously with the experiments to gain valuable insights into Cc sensing mechanisms in many recent materials. For example, the combined experimental and theoretical calculation by Ponnusamy *et al.* found that the supreme charge transfer in the ZnO/RGO nanocomposite resulted in improved Cc sensitivity, where RGO behaves as a catalyst in the whole detection mechanism. The Cc sensitivity in the as-prepared nanocomposite is about 162.04 μA mM cm^{-2} and has a detection limit of 47 nM.[23] Similarly, in another work by Murata *et al.*, the strong Cc adsorption on TiO_2 particles occurs by virtue of enhanced charge transfer from the HOMO of the Cc molecule to the conduction band of TiO_2.[24]

Many commercially accessible sensors are made of conventional materials. Besides low sensitivity and selectivity, the high working temperature of these traditional materials limits the sensor efficiencies. For example, the operating temperature of metal oxide-based sensors is in the range of 200–400°.[25] Therefore, they are now being substituted by novel 2D or 3D nanomaterials. Most polymer-based sensors are one-time sensors as they cannot be reused and are relatively unstable, and their preparation methods are highly cumbersome.[26] It is also found that some of the sensors available in the market are not dynamically stable at room temperature. Graphene is widely recognized as one of the best materials for biomolecule or gas sensing applications. However, it has limited usage in real-time sensors because of its zero bandgap nature.[27] As a result, the scientific world is searching for a new series of low-dimensional nanomaterials with semiconducting properties having high stability, low operating temperature, less power consumption, *etc.*

Theoretical predictions and actual syntheses of several novel 2D materials have resulted in discovering materials with great functionalities. A wide range of biomolecules have been effectively detected using 2D materials like transition metal dichalcogenides (TMDCs),[28,29] MXenes, holey graphene, *etc.* 2D MoS_2 nanosheets deposited with Au and Pt core–shell nanoparticles were employed for the electrochemical detection of glucose from the environment containing typical interfering species, including uric acid, sucrose, lactose and ascorbic acid.[30] First-principles calculations were recently performed to analyze the Cc detection in pristine and metal-doped 2D MoS_2 TMDC. The Cc molecule interacts with the metal dopants in the MoS_2 *via* strong orbital hybridization and charge transport between the O 2p orbitals of Cc and metal d orbitals.[31] Khan *et al.* suggested that 2D hBN, a structural counterpart of graphite, is an excellent electrochemical material for detecting dopamine and uric acid in body fluids.[32] Gouveia *et al.* recently reported the possibility of oxygen terminated 2D Ti_2CO_2 MXene as a nucleobase sensor using DFT. The van der Waals interaction forces are primarily responsible for the nucleobase adsorption on the surface of Ti_2CO_2.[33] Similarly, Yang *et al.* studied the potential of borophene (BP) as a Cc sensor by employing the DFT approach. The Cc molecules adsorb on the BP surface with an energy of −1.35 kcal mol^{-1}. According to the findings, increasing the concentration of Cc molecules does not affect sensor responsiveness. The BP sensor has an additional advantage of a rapid recovery time of 7.6 ns.[34]

Graphyne (GY) is a very recent experimentally synthesized allotrope of carbon whose structure consists of benzene rings joined by ethylenic groups.[35,36] The remarkable properties promote GY to excel in multitudinous applications like energy storage, drug delivery, sensors, *etc.*[37,38] Additionally, the derivatives of GY like graphdiyne[39] and boron-graphdiyne[40] have also been successfully prepared experimentally. Lately, Liu and colleagues synthesized a 2D holey graphyne (hGY) from 1,3,4 tribromo-246-trithynyl benzene *via* Castro–Stephens coupling reactions.[41] The 2D structure of hGY is composed of C–C networks connected alternatively by benzene rings and sp hybridized carbon atoms. The large surface area with

the homogeneous distribution of holes in the 2D system makes it exceptionally stable and unique for myriad applications.[41,42]

To the best of our knowledge, this is the first theoretical work expounding the Cc detection possibilities of the hGY monolayer. Until now, the 2D hGY has been investigated only for hydrogen storage applications.[41–43] Herein, we have employed the first-principles density functional theory method to examine the Cc detection by pristine and transition metal (TM) embedded 2D hGY monolayers. Since the Cc interaction with the pristine hGY monolayer is weak, we have embedded the TMs like Sc, Cu, and Pd on the hGY surface. The TM doping can alter the inherent properties of the hGY and obviously induce a strong chemical interaction between the Cc molecule and the surface of the hGY system.[44] In this study, the three TMs dopants chosen have distant characteristics, *i.e.* Sc belongs to the class of early TMs with $3d^1$ $4s^2$ electronic configuration, whereas Cu and Pd are from late TMs. Pd has a completely filled 3d shell, while Cu has a $3d^{10}$ $4s^1$ electronic configuration. Hence, herein we have considered the TMs with partially filled and completely filled electronic shells. Our findings recommend that the Sc embedded hGY monolayer is the best material for Cc detection due to its higher binding, accelerated charge transport, and strong orbital interactions between the O 2p of Cc molecules and the valence orbital of Sc (4s and 3d). Moreover, we have performed *ab initio* molecular dynamics simulations to verify the structural integrity of the sensor material at 300 K. Our results prove that the proposed hGY system is suitable for devising gas or biomolecule sensors and performs with higher efficiency in terms of sensitivity and selectivity.

Simulation methodology

The structural optimizations and electronic calculations of 2D hGY were carried out with the assistance of VASP software within the Density Functional Theory (DFT) frame. Projector Augmented Plane wave (PAW) potentials within Generalized Gradient Approximation (GGA) were selected to describe the effect of core electrons on the valence electron density.[45,46] For considering the long-range van der Waals (vdW) interactions between Cc and hGY, an empirical correction method of Grimme's DFT-D3 has also been included in this computation.[47] A plane-wave cut-off energy of 500 eV is adopted. During the total energy calculations, atomic movements were permitted in all directions, and the system was allowed to relax until the forces converged below 0.01 eV $Å^{-1}$.

Moreover, the Brillouin zone was sampled by a $6 \times 6 \times 1$ Monkhorst-pack *K*-points grid for structural optimizations and a $9 \times 9 \times 1$ *k*-point grid for density of states calculations (DOS).[48] A 2×2 supercell of 2D hGY was constructed for the entire calculation, sufficient for the Cc adsorption. A vacuum spacing of 20 Å is inserted perpendicular to the *XY* dimensions to ignore the periodic effects in the *Z* direction. The structural integrity of the best system (hGY + Sc) at room temperature is established *via* the *ab initio* MD calculations.[29]

Results and discussion

Analysis of structural and electronic properties of the pristine hGY monolayer

The hGY is a 2D allotrope of carbon having a structural resemblance with graphene with hexagonal symmetry. It belongs to the point group of D_{6h} (No. 27) and the space group of *P*6/*mmm*. In this study, we have used a 2×2 supercell of the pristine hGY monolayer to study Cc adsorption. The DFT optimized structures of both primitive and supercell of 2D hGY are shown in Fig. 1. The crystal lattice of the primitive cell of hGY is hexagonal with 24 C atoms.[41] For the primitive unit cell, the optimized lattice parameters are $a = b = 10.8$ Å and are consistent with the earlier reported theoretical value of 10.85 Å.[43] Each carbon atom in the hGY systems is classified as either type 1-sp^2 hybridized (C1) or type 2-sp hybridized (C2) (refer to Fig. 1(a)), and the system consists of four different C–C bond types: one *sp* hybridized C atom bonded with another sp hybridized C atom, one sp–sp^2 bond and two sp^2–sp^2 C–C bonds (indicated as *b*1, *b*2, *b*3 and *b*4 in Fig. 1(a)). The respective bond distances obtained are *b*1 = 1.225 Å, *b*2 = 1.41 Å, *b*3 = 1.462 Å, and *b*4 = 1.396 Å. This carbon 2D system adopts a pattern of 6 and 8 vertex rings in which the hexagonal rings are linked alternatively *via* the sp hybridized carbon–carbon triple bonds. The calculated bond angle between the hexagon and the –C≡C– is 124°. Hence, the C–C bond distances, bond angles, and lattice parameters are in good congruence with the former theoretical results of *b*1 = 1.227 Å, *b*2 = 1.414 Å, *b*3 = 1.463 Å, *b*4 = 1.397 Å and ≤ 125.8°.[42] The electronic structure of pristine monolayer hGY is also explored by examining the total DOS. The DOS plot in Fig. 1(d) explicitly reveals that hGY is a semiconductor with a bandgap of 0.52 eV. This value is comparable with the theoretically reported bandgap of 0.5 eV.[42] The non-magnetic nature of hGY is also reflected in the symmetric electronic spin states near the Fermi level of the DOS plot. It should be noted that the electronic properties before and after the biomolecule adsorption are more critical for analyzing the sensing properties of the system under study.

Catechol adsorption performance of the pristine hGY monolayer

To attain the best stable configuration for Cc adsorption on the hGY monolayer, we have tried a variety of adsorption models. For instance, the Cc molecule is placed ∼2 Å above, parallelly or vertically at different adsorption sites of the monolayer. The hGY monolayer has 11 adsorption sites (C, P1, P2, H, O, above b1, b2, b3 and b4, above the C1 and C2 sites) which are indicated in Fig. 1(b). Binding energy, bond distances, and charge transfer can decide whether the adsorption is chemical or physical.

The binding energy (E_{BE}) of the Cc molecule with the hGY system is calculated by the expression given below:

$$E_{BE} = E_{hGY+Cc} - (E_{hGY} + E_{Cc}) \quad (1)$$

Here, E_{hGY+Cc}, E_{hGY} and E_{Cc} refer to the isolated energies of the hGY + Cc system, the hGY supercell and the Cc molecule,

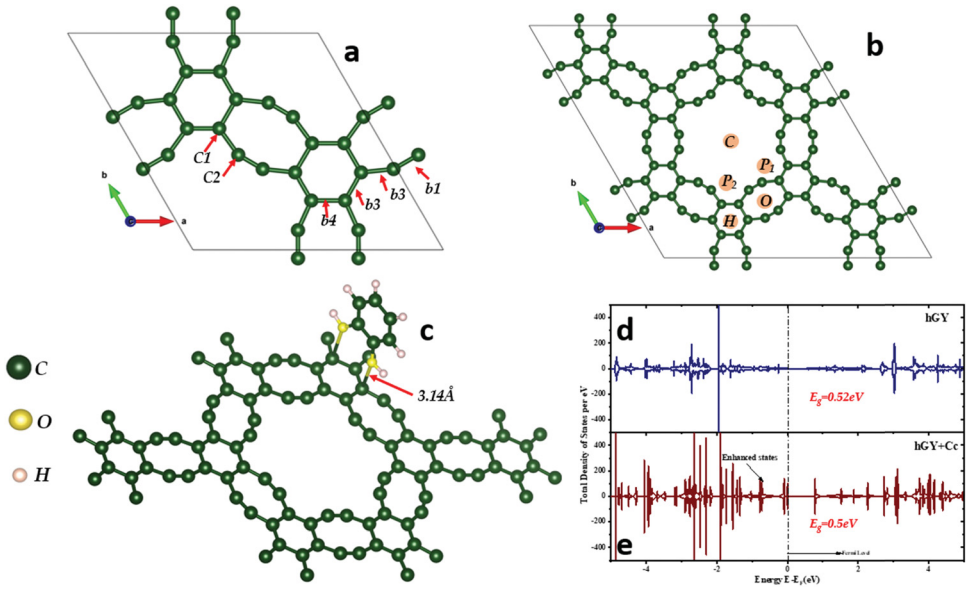

Fig. 1 Optimized geometries of the (a) primitive unit cell, (b) 2 × 2 monolayer of hGY and (c) catechol adsorbed hGY monolayer. Total DOS of (d) pristine hGY and (e) the Cc adsorbed hGY monolayer. Eleven adsorption sites, namely, C: central, P_1 and P_2: porous, O: octagonal, H: hexagonal, b1, b2, b3, b4, C1 and C2 sites, are considered. The vertical dotted line in the DOS plot (d) and (e) indicates the Fermi level and is set to zero eV.

respectively. The more negative the binding energy, the stronger the adsorption, and the greater the stability. In contrast, positive E_{BE} implies that the process is endothermic, and the molecule may not adsorb on the material surface. After the complete optimization, the most favourable adsorption configuration is found to be one in which the Cc molecule is vertically aligned above the hexagonal site (Fig. 1(c)), with a maximum binding energy of −0.702 eV. The shortest bond separation between the O atom of Cc and the sp^2 hybridized carbon atom is 3.14 Å. We notice that after the optimization, the flat-lying Cc molecule shifts to the H site when placed initially at b1, b2, and C1 positions and to the O site from P1, P2, b3, b4, C and C2 positions. Similarly, the vertically standing Cc molecule moves to the H site from the C, P1, P2, and C2 sites after the optimisation. The DFT optimized structures of the Cc molecule vertically adsorbed at O and b4 sites and horizontally adsorbed above the O and H sites are included in Fig. S1 (ESI†). Their binding energies and distances are also tabulated (Table S1, ESI†).

Analysis of total and partial density of states. To better comprehend the adsorption properties, we have plotted the total DOS of the hGY + Cc system in Fig. 1(e). The adsorption of Cc introduced an enhancement in the energy states below the Fermi level. In addition, the separation between the conduction band minima and the valence band maxima gets slightly narrowed from 0.52 eV to 0.50 eV after the adsorption process. The partial density of states (PDOS) plot in Fig. S2 (ESI†) details the effect of Cc adsorption at the orbital level. The increased energy levels of the C 2p orbitals of the hGY system below the Fermi level suggest that hGY gains charge from the Cc molecule. The same is confirmed by the decrease in the energy states of O 2p orbitals of the Cc molecule at the Fermi level. Therefore, the PDOS plot explicates the orbital interactions between the C 2p in hGY and the O 2p orbitals of Cc during the adsorption process.

Bader charge analysis. The extent of charge transfer between the Cc molecule and the C atoms of hGY can be determined quantitatively by performing the Bader charge analysis[49] and is expressed mathematically by the equation given below:

$$\Delta q' = q'(\text{hGY + Cc}) - q'(\text{hGY}) - q'(\text{Cc}) \qquad (2)$$

where q' is the charge of respective systems.

In the hGY + Cc system, the Cc molecule loses only a negligible charge of 0.07e to the hGY system. In the case of physisorption, the binding of the molecules on the surface will be weak, and there might not be any transfer of charges. As a result, we can conclude that the Cc interaction with the pristine hGY is mostly physisorption. Therefore, adopting any adsorption ability improvement method will be a bonus.

Transition metal embedded hGY. The pristine hGY does not exhibit sufficient sensitivity towards Cc molecules since the adsorption between Cc and hGY is mostly physisorption, and the binding is rather weak. Intentional doping by TMs is one of the best-accepted strategies to upgrade the sensing ability of the substrate material. We have introduced the TMs Sc, Pd and Cu above 2 Å at all the adsorption sites of hGY and are geometrically optimized to obtain a minimum energy configuration.

Binding energy determines the most suitable adsorption site for the metal dopant, and it is computed similarly as before by the equation

$$E_{BE} = E_{hGY+TM} - (E_{hGY} + E_{TM}), \qquad (3)$$

where E_{hGY+TM}, E_{hGY} and E_{TM} are the isolated energies of the TM embedded hGY system, the hGY supercell and the TM, respectively. The binding energies and the bond distances of the TM embedded systems are given in Table 1.

Table 1 Binding energy, bandgap, bond distances and charge transfer in different configurations of hGY

System	Binding energy (eV)	Energy gap (eV)	Bond distance (Å)	Charge transfer (e)
hGY		0.52		
hGY + Cc	−0.702	0.5	d_{C-O} = 3.14	−0.07
hGY + Sc	−4.09	0	d_{C1-Sc} = 2.44 d_{C2-Sc} = 2.21	−1.89
hGY + Cu	−1.42	0	d_{C1-Cu} = 2.74 d_{C2-Cu} = 2.19	−0.65
hGY + Pd	−0.692	0.45	d_{C1-Pd} = 2.23 d_{C2-Pd} = 2.41	−0.34
hGY + Sc + Cc	−3.22	0	d_{Sc-O} = 2.2	0.9
hGY + Cu + Cc	−3.2	0	d_{Cu-O} = 2.202	0.13
hGY + Pd + Cc	−1.28	0.4	d_{Pd-O} = 2.26	0.089

As per the calculation, the favourable site with maximum binding energy for Sc and Cu appears to be above the centre of the octagonal site, whereas for Pd, it is above the b4 site. The structures of the TM embedded hGY after optimization, along with the bond distances (TM–C1, TM–C2), are shown in Fig. 2(a) and Fig. S3 (ESI†). Among the three metals, Sc binds strongly with the hGY surface, followed by Cu and Pd. The calculated E_{BE} of Sc on the octagonal site is −4.09 eV, and the corresponding distances to C1 and C2 are 2.44 Å and 2.21 Å, respectively. Both the energy and bond distance match well the previous results.[42] For the case of Cu, the binding energy and the bond distances C1–Cu and C2–Cu are −1.42 eV and 2.74 Å and 2.16 Å, respectively. Pd binds weakly on the hGY system with −0.692 eV, and the C1–Pd bond distance is 2.23 Å and C2–Pd is 2.41 Å.

Binding mechanism of TM with hGY

Profound knowledge of the interaction mechanism of TMs with the hGY can be acquired by investigating their electronic structure, charge transfer and orbital interactions through total DOS, partial DOS, charge density distribution, Bader analysis, *etc.*

Analysis of total density of states. Fig. 3 depicts the total DOS plots of the TM embedded hGY system, which promote examining the differences in the physical properties of the system. As mentioned previously, the pristine hGY is semiconducting with a 0.52 eV bandgap. After Sc and Cu doping, the semiconducting nature of the pristine hGY turned metallic with a zero bandgap, *i.e.* metal doping dramatically increased the conductivity, which is significant for biomolecule detection. The slight asymmetric up and down spin states near the Fermi level of the Sc + hGY system signify the non-zero magnetic moment. This is because of the presence of unpaired electrons in the 3d valence orbital of Sc. The calculated moment is 1 μB. For the case of Pd doping, the low binding energy retained the semiconducting properties of the hGY but reduced the band gap to 0.45 eV.

Analysis of partial density of states. To understand the orbital level binding and charge transfer mechanism, we analyzed the PDOS of pristine and the TM embedded hGY. The left panel of the PDOS plots (Fig. 4 and Fig. S5, ESI†) compares the C 2p orbitals of pristine and metal embedded hGY, whereas the right panel compares the valence orbitals of the isolated TM atom and the TM in TM embedded hGY. Considering the PDOS of the Sc doped hGY system (in Fig. 4), we can see that some new energy states are originated near the Fermi level of C 2p orbitals, which are missing in the C 2p of the pristine system, implying that the charge is transferred from the Sc to C 2p orbitals. The subsequent reduction in the intensity of energy states near the Fermi level of both 3d and 4s orbitals of Sc in the Sc + hGY system than in the isolated Sc metal confirms the charge transfer from the Sc valence orbitals to C 2p orbitals.

A similar charge transfer and orbital interaction can be seen in the case of Cu and Pd doped hGY (see the PDOS plot in

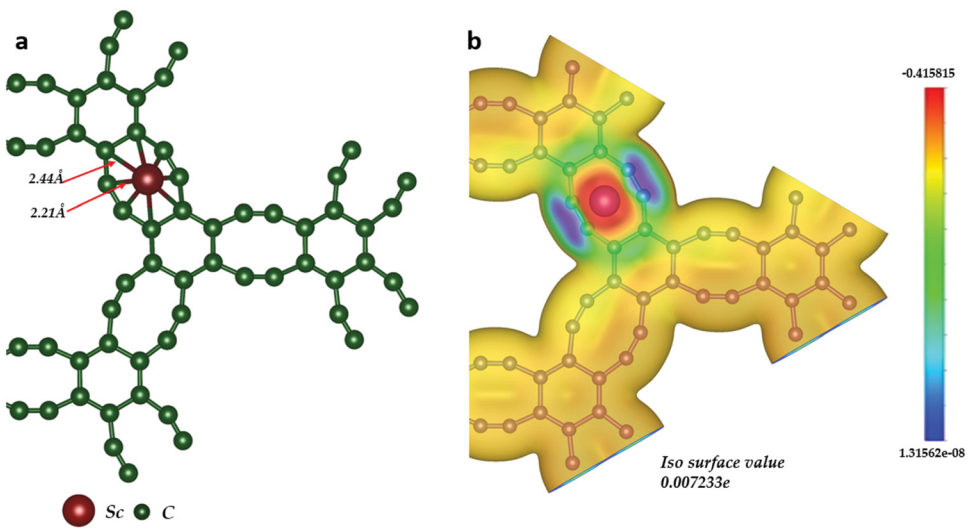

Fig. 2 (a) Top view of most stable adsorption geometries of the Sc embedded hGY monolayer. The bond distance of Sc with the two types of C atoms is also depicted. (b) Charge density difference plot (cdd) of hGY + Sc systems. The corresponding iso surface values are indicated in the figure. The blue and green regions represent charge gain, whereas the red colour denotes the charge loss.

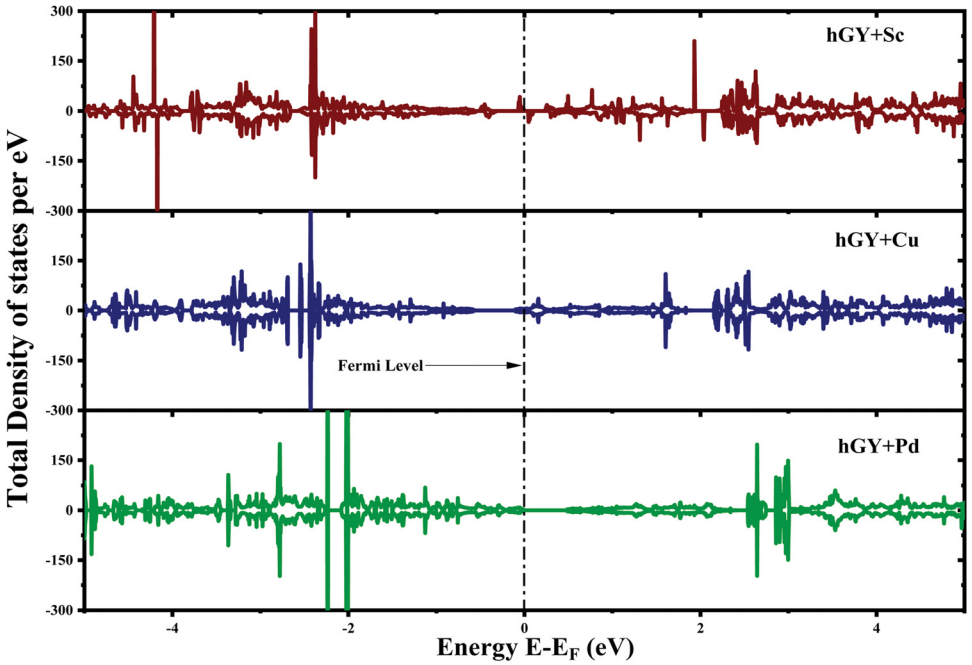

Fig. 3 Total DOS plots of TM (Sc, Cu and Pd) embedded hGY.

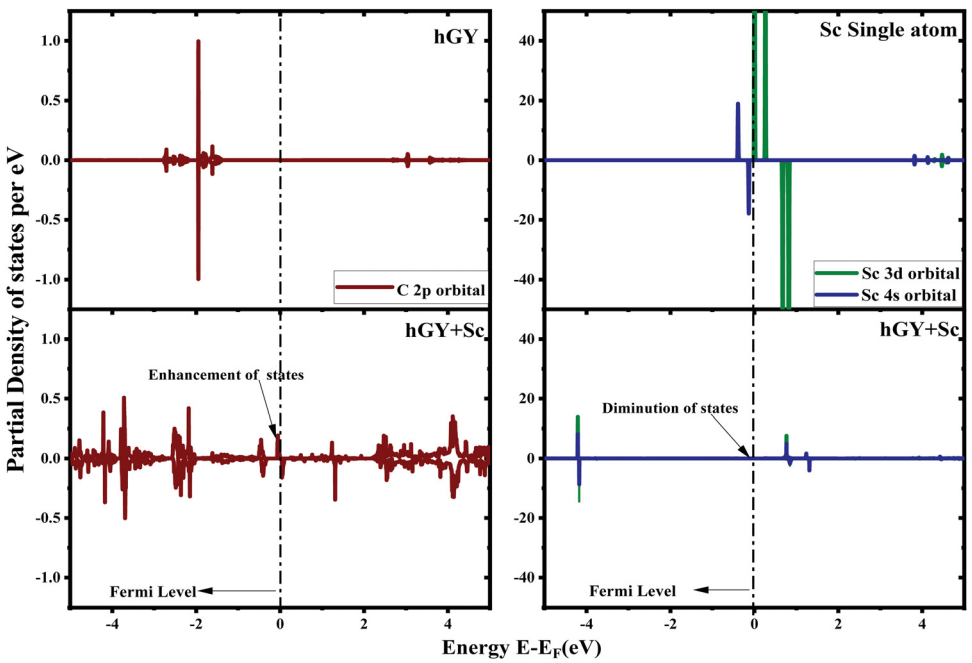

Fig. 4 Partial density of states plots: the left panel compares the C 2p orbitals in hGY to those in Sc embedded hGY, and the right panel compares the valence orbitals of Sc in the isolated atom to that in the Sc embedded hGY system.

Fig. S5a and b, ESI†). The TM doping induces additional energy states in the valence band of C 2p orbitals in hGY + Cu and increases the intensity of energy states in the conduction band of C 2p orbitals in hGY + Pd. Besides, a remarkable diminution of energy states at the Fermi level of Cu 4s and Pd 3d orbitals in Cu and Pd embedded hGY, respectively, highlights the charge transfer from the valence orbital of TM to C 2p orbitals. Hence, the charge enrichments and depletions near the Fermi level of the C 2p orbitals and valence orbitals of the TMs, respectively, validate the strong hybridization between the TMs and hGY.

Bader charge analysis. The charge transfer between the metal and the hGY system can be quantified using the expression

$$\Delta q' = q'(\text{hGY + TM}) - q'(\text{hGY}) - q'(\text{TM}) \quad (4)$$

The positive value in the above equation implies that the charge transfer occurs from the metal atom to the hGY system. The more significant the amount of charge transferred between the TM and hGY, the greater the binding of TM on the hGY system. As per the calculation, Sc loses about 1.89*e* charge to C 2p orbitals of hGY. These large amounts of charges are contributed by 3d and 4s orbitals of Sc. On the other hand, Cu 4s and Pd 4d orbitals lose a total amount of 0.65*e* and 0.34*e* charges, respectively, to the hGY system. Hence, the Bader analysis confirms that, in comparison with the other two TMs, Sc can form stable bonds with the C atoms and strongly binds to the hGY system.

Charge density distribution plot. The charge transferring path while TM binds on the hGY surface can be visualized by plotting the charge density difference (cdd). Mathematically the cdd can be represented as

$$\Delta\rho = \rho(\text{hGY + TM}) - \rho(\text{hGY}) \quad (5)$$

where ρ is the charge density.[28,50,51]

The green, blue and red colours in the cdd plot (Fig. 2(b) and Fig. S4, ESI†) refer to the regions with small charge gain and significant charge gain and charge depletion, respectively. The charge deficit region occurs around the TM atom, signifying its tendency to donate charges. Hence, the cdd plot confirms the results obtained quantitatively *via* Bader analysis.

Catechol adsorption performance of the TM embedded hGY monolayer

The Cc molecule is placed approximately 2 Å above the TM (Sc, Cu and Pd) in the TM embedded hGY systems and is geometrically optimized to obtain the minimum energy configuration. Fig. 5 shows the DFT optimized structures. The shortest bond distance between the Cc molecule and the TMs in TM + hGY is also included in Fig. 5. The binding energy of Cc on different TM embedded hGY can be calculated using the equation

$$E_{BE} = E_{\text{hGY+TM+Cc}} - (E_{\text{hGY+TM}} + E_{Cc}) \quad (6)$$

which is similar to eqn (1). The binding energies of Cc on different systems, along with the adsorption distances, are tabulated (Table 1). The Cc molecule strongly adsorbs on the Sc embedded hGY with a binding energy of −3.22 eV at a bond distance of (d_{Sc-O}) = 2.2 Å. Meanwhile, it binds on the Cu and Pd embedded hGY with the binding energies of −3.2 eV and −1.28 eV, respectively. Their corresponding bond distances are d_{Cu-O} = 2.02 Å and d_{Pd-O} = 2.26 Å. Hence, Cc shows strong adsorption on the TM doped hGY compared to the pristine hGY.

Adsorption mechanism of Catechol on TM embedded hGY

The charge transfer and orbital interactions can lead to drastic changes in the electronic properties of the TM embedded hGY system after Cc adsorption, which can be determined from the DOS plots. Meanwhile, the PDOS and Bader analysis could reveal the orbital mixing and the extent of charge flow.

Analysis of total density of states. The DOS calculation is essential for examining the electronic behaviour of the interaction between Cc and the TM embedded hGY system. Fig. S6 (ESI†) describes the total DOS plots of the Cc adsorbed TM embedded hGY. The Cc adsorption increased the intensity of peaks below the Fermi level (−4 eV to 0 eV) of the hGY + TM + Cc system. The asymmetric spin states at the Fermi level indicate that the hGY + Sc system maintains the magnetic characteristics even after Cc adsorption.

Analysis of partial density of states. The left panels of the PDOS plots in Fig. 6 and Fig. S7 (ESI†) compare the valence orbitals of TMs (Sc, Cu, and Pd) in hGY + TM and hGY + TM + Cc systems. In contrast, the right panels compare the O 2p orbitals of the isolated Cc molecule and the hGY + TM + Cc system. The Cc interaction with the hGY + Sc system depleted some energy states near the Fermi level of O 2p orbitals, which existed in the isolated Cc molecule (Fig. 6). This explains that the charge transfer occurs from the orbitals of O in Cc. The enrichment of states below the Fermi level of 4s and 3d Sc orbitals in hGY + Sc + Cc highlights the charge gained by the Sc atom. Therefore, the strong adsorption of Cc with the hGY + Sc system is mainly due to the charge transport from O 2p to Sc 4s and 3d orbitals.

A similar charge transfer can also be observed when the Cc molecule interacts with the Pd embedded hGY systems (Fig. S7b, ESI†). The O 2p orbital of the Cc molecule loses a significant amount of charges to the 3d orbitals of Pd.

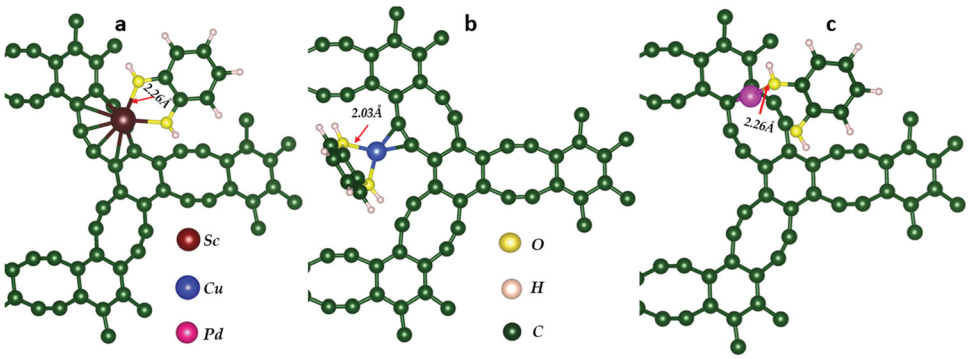

Fig. 5 Top view of most stable adsorption geometries of the Cc molecule adsorbed on the (a) Sc embedded, (b) Cu, and (c) Pd embedded hGY monolayer.

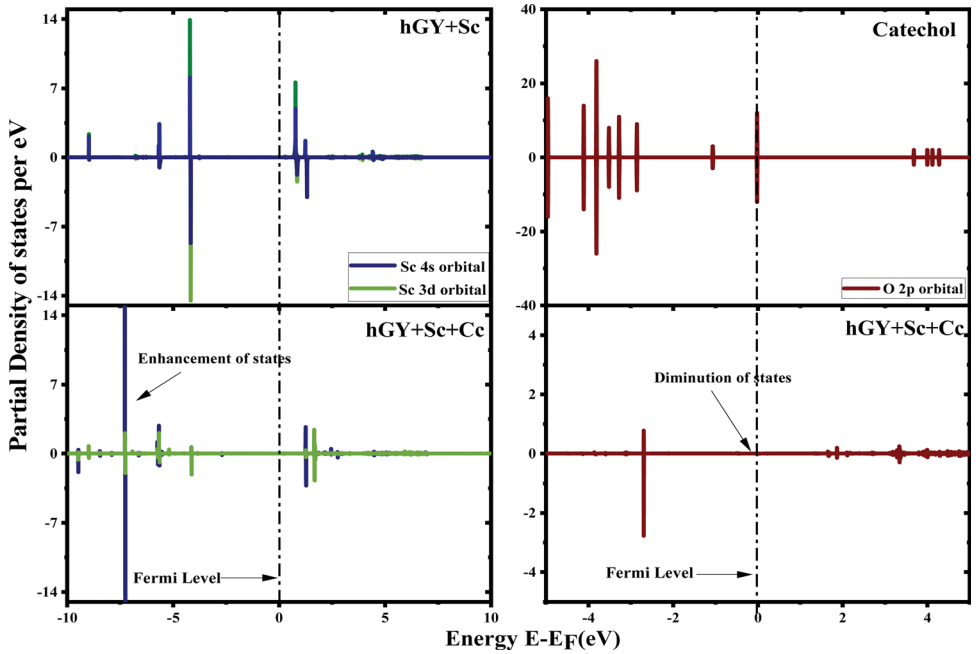

Fig. 6 Partial density of state plots comparing the valence orbitals of Sc (left panel) and Cc (right panel) in hGY + Sc and hGY + Sc + Cc systems.

The missing energy states in the O 2p orbitals and improved energy states in the valence orbitals of Pd in the hGY + Pd + Cc system near the Fermi level make clear this charge transfer. In contrast, the charge gained by 4s orbitals of Cu in the hGY + Cu system from the O 2p of Cc is redistributed to the nearby C 2p orbitals. This is explicit from the declined energy states of Cu 4s and enriched states of C 2p orbitals in the valence band of the hGY + Cu + Cc system in Fig. S7a (ESI†). In conclusion, the PDOS calculation gives a complete picture of orbital hybridization and charge transfer between the O 2p of Cc and valence orbitals of the TMs when the Cc molecules interact with the hGY + TM system.

Bader charge analysis. According to the Bader charge analysis, the O 2p orbital of the Cc molecule loses an overall charge of 0.9*e* to the hGY + Sc system. At the same time, 0.53*e* and 0.089*e* charges are transported from the O 2p orbital to hGY + Cu and hGY + Pd systems, respectively. This charge loss is quite consistent with the PDOS results and mirrors the charge donating nature of the Cc molecule. The comparatively large binding energy, binding distances, charge transfer and evident changes in the electronic orbitals indicate the strong chemisorption of the Cc molecule on the TM-embedded hGY system. The charge transfer in the magnetic system will be higher. That is why the charge transfer between the Cc molecule and the hGY + Sc system is very high compared to the other two TM doped systems. The higher the charge transfer between Cc and hGY + Sc, the greater the sensitivity of hGY. Charge transfer and binding energy calculations suggest that the Sc embedded hGY can be the best material for Cc detection. The charge transfer in each system is listed in Table 1.

Practicability of the hGY + TM-based catechol sensor

Structural integrity. Since the DFT simulations are carried out at 0 K, *ab initio* molecular dynamic simulations were performed to inspect the structural integrity of the Sc embedded hGY system at room temperature. Generally, desorption of the molecules requires heating of the system to ambient temperatures. If the hGY system maintains its structural stability at higher temperatures, the desorption of the molecules from its surface can be easily attained. The time for MD simulation was set to 5 ps within a 1 fs time step, and the structural variations were determined by varying the temperature from 0 K to 300 K. The final structure at 300 K is shown in Fig. 7. The figure shows that at 300 K, the Sc atom remains intact on the surface of the hGY surface with minor bond length variations. Then the resultant structure is allowed to achieve an equilibrium temperature of 300 K for 3 ps. The Sc–C bond distance *versus* time step at a constant temperature of 300 K is plotted to examine the fluctuations in bond distances in the hGY + Sc system (Fig. 8). It is evident from the plot that the bond distance Sc–C remains stable during the simulation and oscillates about an average of 2.203 Å. The above results confirm that the Sc embedded hGY system is thermodynamically stable at room temperature. The sensor should be reusable for its practical application.

The catechol molecule partially decomposes at 200 °C, and at 300–350 °C, it completely decomposes.[52] Therefore it would be feasible to reboot the sensor without heating it to extremely higher temperatures, which is expected due to the large adsorption energies. Other approaches, like UV irradiation,[53] exposing the sensor to a humid atmosphere, *etc.*, can also drive the desorption process by evading the heating procedure.

Sensing parameters

Experimentally, the sensing parameters include the limit of detection (LOD), sensitivity, selectivity, repeatability, S/N ratio, *etc.* From the theoretical point of view, binding or adsorption

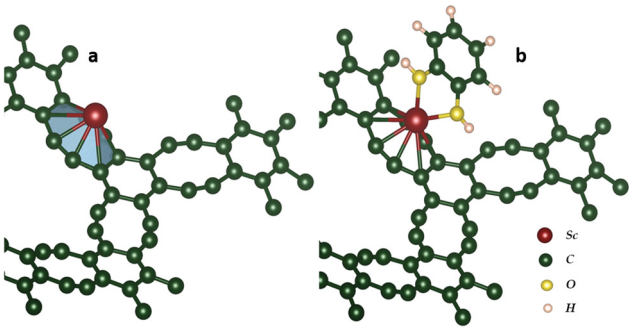

Fig. 7 MD snapshot of (a) hGY + Sc and (b) hGY + Sc + Cc systems at 300 K for 5 ps.

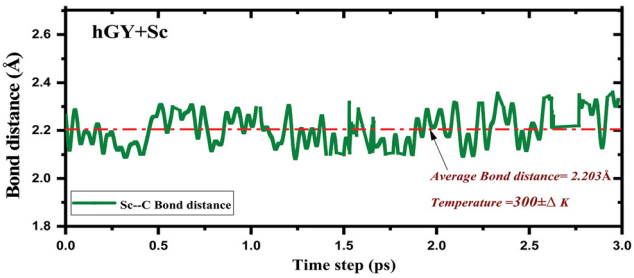

Fig. 8 Variation of the bond distance between Sc and C in the hGY system at an equilibrium temperature of 300 K. The horizontal dotted line denotes the average bond distance.

energy, adsorption distance, charge transfer, *etc.*, are the parameters that determine the response of a sensor material.

Binding energy and distance. The E_{BE} and binding distances of the molecules on the material substrate are inversely related. An increase in E_{BE} results in a decrease in the distance of adsorption of the molecule. The E_{BE} symbolizes the extent to which the Cc molecule adsorbs on the pristine or doped hGY surface. According to our calculations, the Cc molecule adsorbs strongly on the Sc embedded hGY with a E_{BE} value of -3.22 eV at a distance of 2.2 Å, whereas it weakly adsorbs on the pristine hGY with E_{BE} value of -0.702 eV.

Charge transfer. The adsorption performance of the hGY-based sensor material is generally based on the charge transfer between Cc molecules and the pristine or doped hGY system. Hence, the efficient control of this charge transfer between the molecule and the hGY can regulate the sensitivity. The higher the charge transfer between the molecule and the substrate, the higher will be the adsorption strength. In our study, the higher binding of Cc with the Sc embedded hGY system is mainly due to the extensive charge transfer (0.9*e*) between Cc and the Sc embedded hGY.

Conclusion

The catechol (Cc) adsorption performance and sensing mechanism of pristine and TM (Sc, Cu and Pd) embedded holey graphyne (hGY) were explored by employing the first-principles density functional theory method. The total DOS, PDOS and Bader charge analyses were performed to inspect the changes in the electronic structure, orbital interactions and charge transfer, respectively, after Cc adsorption. Though the Cc molecule adsorbs weakly on the surface of the hGY, the addition of TM dopants strengthened the adsorption process by increasing the conductivity. Sc and Cu dopants turned the hGY metallic. Pd doping doesn't induce any changes in its semiconducting nature. In addition, the Sc atom generates a slight magnetism in the hGY system because of the presence of an unpaired electron in its 3d and 4s electron orbitals. Among the three TMs, Sc has a strong binding with the hGY. The Cc molecule could stably adsorb on the TM embedded hGY, and the adsorption process is mostly chemisorption. Our current study expects the Sc embedded hGY to have an excellent adsorption performance towards the Cc molecule. Besides the high binding energy of Cc with hGY + Sc, there is a strong orbital hybridization and charge transfer between the O 2p orbitals of the Cc molecule and the valence orbitals of the Sc dopant. The structural integrity of the system at ambient temperature has also been confirmed *via* MD simulations. Therefore, the Sc embedded hGY is predicted to be a potential material for developing high-performance biomolecule sensors, particularly catechol sensors.

Conflicts of interest

There are no conflicts to declare.

Acknowledgements

KNK acknowledges SERB: CRG (Grant No. CRG/2021/001506), Government of India programmes for providing the facilities for research and development in IIUCNN, MGU. The authors, B. C., S. L. and A. K., would like to thank Dr Nandini Garg, Dr T. Sakuntala, Dr S.M. Yusuf and Dr A.K Mohanty for their encouragement and support and the staff of the computer division of BARC for providing access to the supercomputing facility. BC thanks Beetihotra Chakraborty for the help.

References

1 Y. Xia, K. Wang, Y. Shi, X. Gui, C. Lv and H. Tao, *FlatChem*, 2021, **25**, 100214.
2 M. Buleandra, A. A. Rabinca, C. Mihailciuc, A. Balan, C. Nichita, I. Stamatin and A. A. Ciucu, *Sens. Actuators, B*, 2014, **203**, 824–832.
3 R. Saravanan, N. Karthikeyan, V. K. Gupta, E. Thirumal, P. Thangadurai, V. Narayanan and A. Stephen, *Mater. Sci. Eng., C*, 2013, **33**, 2235–2244.
4 M. Ghalkhani, N. K. Bakirhan and S. A. Ozkan, *Crit. Rev. Anal. Chem.*, 2020, **50**, 538–553.
5 L. Wang, P. Huang, J. Bai, H. Wang, L. Zhang and Y. Zhao, *Int. J. Electrochem. Sci.*, 2006, **1**(3), 238–249.
6 I. J. B. J. o. C. Purchase, 1978, 37, 649.
7 J. A. Young, *J. Chem. Educ.*, 2005, **82**, 31.
8 M. Hirose, S. Fukushima, H. Tanaka, E. Asakawa, S. Takahashi and N. Ito, *Carcinogenesis*, 1993, **14**, 525–529.

9 U. D. o. Health and N. L. o. M. Human Services %J National Toxicology Information Program, Bethesda, MD, 1993.
10 B. Pérez López and A. Merkoçi, *Analyst*, 2009, **134**, 60–64.
11 V. Zucolotto, A. P. Pinto, T. Tumolo, M. L. Moraes, M. S. Baptista, A. Riul, Jr., A. P. Araújo and O. N. Oliveira, Jr., *Biosens. Bioelectron.*, 2006, **21**, 1320–1326.
12 A. Pathak and B. D. Gupta, *ACS Appl. Nano Mater.*, 2020, **3**, 2582–2593.
13 S. Nsanzamahoro, F. P. Mutuyimana, Y. Han, S. Ma, M. Na, J. Liu, Y. Ma, C. Ren, H. Chen and X. Chen, *Sens. Actuators, B*, 2019, **281**, 849–856.
14 S. Veeralingam and S. Badhulika, *Mater. Sci. Eng., C*, 2020, **108**, 110365.
15 G. Marrubini, E. Calleri, T. Coccini, A. F. Castoldi and L. Manzo, *Chromatographia*, 2005, **62**, 25–31.
16 S. R. Nambiar, P. K. Aneesh and T. P. Rao, *Analyst*, 2013, **138**, 5031–5038.
17 M. R. Nezhad, M. Alimohammadi, J. Tashkhourian and S. M. Razavian, *Spectrochim. Acta, Part A*, 2008, **71**, 199–203.
18 J. Lasovsky, J. Hrbac, D. Sichertova and P. Bednar, *Luminescence*, 2007, **22**, 501–506.
19 R. Saravanan, E. Thirumal, V. K. Gupta, V. Narayanan and A. Stephen, *J. Mol. Liq.*, 2013, **177**, 394–401.
20 J. Ahmed, M. Faisal, M. Jalalah, M. Alsaiari, S. A. Alsareii and F. A. Harraz, *Colloids Surf., A*, 2021, **619**, 126469.
21 Y. Dang, Y. Zhai, L. Yang, Z. Peng, N. Cheng and Y. Zhou, *RSC Adv.*, 2016, **6**, 83994–84002.
22 L. Zhao, J. Yu, S. Yue, L. Zhang, Z. Wang, P. Guo and Q. Liu, *J. Electroanal. Chem.*, 2018, **808**, 245–251.
23 R. Ponnusamy, R. Venkatesan, A. Gangan, R. Samal, B. Chakraborty, D. J. Late and C. S. Rout, *Appl. Surf. Sci.*, 2019, **495**, 143588.
24 Y. Murata, H. Hori, A. Taga and H. Tada, *J. Colloid Interface Sci.*, 2015, **458**, 305–309.
25 C. Wang, L. Yin, L. Zhang, D. Xiang and R. Gao, *Sensors*, 2010, **10**, 2088–2106.
26 H. Bai and G. Shi, *Sensors*, 2007, **7**, 267–307.
27 H. Huang, S. Su, N. Wu, H. Wan, S. Wan, H. Bi and L. Sun, *Front. Chem.*, 2019, **7**, 399.
28 A. Vaidyanathan, S. Lakshmy, G. Sanyal, S. Joseph, N. Kalarikkal and B. Chakraborty, *Appl. Surf. Sci.*, 2021, **550**, 149395.
29 G. Sanyal, S. Lakshmy, A. Vaidyanathan, N. Kalarikkal and B. Chakraborty, *Surf. Interfaces*, 2022, **29**, 101816.
30 S. Su, Z. Lu, J. Li, Q. Hao, W. Liu, C. Zhu, X. Shen, J. Shi and L. Wang, *New J. Chem.*, 2018, **42**, 6750–6755.
31 S. Lakshmy, G. Sanyal, A. Vaidyanathan, S. Joseph, N. Kalarikkal and B. Chakraborty, *Appl. Surf. Sci.*, 2021, **562**, 150216.
32 A. F. Khan, D. A. C. Brownson, E. P. Randviir, G. C. Smith and C. E. Banks, *Anal. Chem.*, 2016, **88**, 9729–9737.
33 J. D. Gouveia, G. Novell-Leruth, F. Viñes, F. Illas and J. R. B. Gomes, *Appl. Surf. Sci.*, 2021, **544**, 148946.
34 R. Yang, C. Wu and S. Ebrahimiasl, *J. Mol. Model.*, 2021, **27**, 310.
35 Y. Li, L. Xu, H. Liu and Y. Li, *Chem. Soc. Rev.*, 2014, **43**, 2572–2586.
36 Q. Li, Y. Li, Y. Chen, L. Wu, C. Yang and X. Cui, *Carbon*, 2018, **136**, 248–254.
37 J. Kang, Z. Wei and J. Li, *ACS Appl. Mater. Interfaces*, 2019, **11**, 2692–2706.
38 J. Wang, H. Shi, W. Wang, Z. Xu, C. Hong, Y. Xue and F. Tian, *Chem. Eng. J.*, 2022, **432**, 133617.
39 X. Gao, H. Liu, D. Wang and J. Zhang, *Chem. Soc. Rev.*, 2019, **48**, 908–936.
40 B. Mortazavi, M. Shahrokhi, X. Zhuang and T. Rabczuk, *J. Mater. Chem. A*, 2018, **6**, 11022–11036.
41 X. Liu, S. M. Cho, S. Lin, E. Yun, E. H. Baek, Z. Chen, D. H. Ryu and H. J. Lee, arXiv preprint arXiv:.03534, 2019.
42 V. Mahamiya, A. Shukla, N. Garg and B. Chakraborty, *Int. J. Hydrogen Energy*, 2022, **47**, 7870–7883.
43 Y. Gao, H. Zhang, H. Pan, Q. Li and J. Zhao, *Nanotechnology*, 2021, **32**, 215402.
44 J. Du, C. Xia, W. Xiong, X. Zhao, T. Wang and Y. Jia, *Phys. Chem. Chem. Phys.*, 2016, **18**, 22678–22686.
45 J. Hafner, 2008, **29**, 2044–2078.
46 K. A. Baseden and J. W. Tye, *J. Chem. Educ.*, 2014, **91**, 2116–2123.
47 S. Grimme, *J. Comput. Chem.*, 2006, **27**, 1787–1799.
48 K. Choudhary and F. J. C. Tavazza, *Comput. Mater. Sci.*, 2019, **161**, 300–308.
49 W. Tang, E. Sanville and G. Henkelman, *J. Phys.: Condens. Matter*, 2009, **21**, 084204.
50 V. Mahamiya, A. Shukla and B. Chakraborty, *Int. J. Hydrogen Energy*, 2022, **47**(12), 7870–7883.
51 B. Chakraborty, P. Ray, N. Garg and S. Banerjee, *Int. J. Hydrogen Energy*, 2021, **46**, 4154–4167.
52 Y. Cheng, Q. Xu, J. Liu, C. Zhao, F. Xue and Y. Zhao, *J. Braz. Chem. Soc.*, 2014, **25**(11), 2102–2107.
53 E. Muckley, A. Nelson, C. Jacobs and I. Ivanov, *Effect of UV irradiation on adsorption/desorption of oxygen and water on carbon nanotubes*, SPIE, 2016.